

“Skinny Milky Way please”, says Sagittarius

S.L.J. Gibbons^{1*}, V. Belokurov¹ and N.W. Evans¹

¹*Institute of Astronomy, University of Cambridge, Madingley Road, Cambridge, CB3 0HA, UK*

Accepted 2014 September 22. Received 2014 September 19; in original form 2014 June 6

ABSTRACT

Motivated by recent observations of the Sagittarius stream, we devise a rapid algorithm to generate faithful representations of the centroids of stellar tidal streams formed in a disruption of a progenitor of an arbitrary mass in an arbitrary potential. Our method works by releasing swarms of test particles at the Lagrange points around the satellite and subsequently evolving them in a combined potential of the host and the progenitor. We stress that the action of the progenitor’s gravity is crucial to making streams that look almost indistinguishable from the N-body realizations, as indeed ours do. The method is tested on mock stream data in three different Milky Way potentials with increasing complexity, and is shown to deliver unbiased inference on the Galactic mass distribution out to large radii. When applied to the observations of the Sagittarius stream, our model gives a natural explanation of the stream’s apocentric distances and the differential orbital precession. We, therefore, provide a new independent measurement of the Galactic mass distribution beyond 50 kpc. The Sagittarius stream model favours a light Milky Way with the mass $4.1 \pm 0.4 \times 10^{11} M_{\odot}$ at 100 kpc, which can be extrapolated to $5.6 \pm 1.2 \times 10^{11} M_{\odot}$ at 200 kpc. Such a low mass for the Milky Way Galaxy is in good agreement with estimates from the kinematics of halo stars and from the satellite galaxies (once Leo I is removed from the sample). It entirely removes the “Too Big To Fail Problem”.

Key words: Galaxy: halo – Galaxy: fundamental parameters – Galaxy: kinematics and dynamics – galaxies: dwarf: Sagittarius

1 INTRODUCTION

Over many years, the uncertainty with which the total mass of the Milky Way is known has been vexing theorists and observers alike. The spread of allowed masses covers a large range of possibilities in which both light ($< 10^{12} M_{\odot}$) and heavy ($> 2 \times 10^{12} M_{\odot}$) Galaxies are permitted to exist. Attempts to gauge the Galactic matter budget have been made using a variety of stellar kinematic tracer populations (see e.g. Smith et al. 2007; Xue et al. 2008; Bovy et al. 2012). However, these methods suffer from systematics caused by the lack of reliable tangential velocity and distance measurements. For non-rotating populations, this is exacerbated by the paucity of fast-moving and/or distant tracers. For a dataset covering a large variety of sight-lines, the need for tangential velocities for every star can be alleviated by using an assumption as to the velocity anisotropy for the population as a whole. The line of sight velocity contains contributions from both the radial and tangential velocities as judged from the Galactic centre. Provided the population is relatively nearby, say at most ~ 50 kpc away, then the veloc-

ity anisotropy can be usefully constrained and some of the degeneracy in mass estimates broken (Deason et al. 2012).

Other attempts at mass measurement have used the motion of the population of the Galactic dwarf satellites and globular clusters (e.g. Little & Tremaine 1987; Zaritsky et al. 1989; Wilkinson & Evans 1999; Sakamoto et al. 2003; Watkins et al. 2010). These have the capability to probe the mass of the Milky Way to much larger radii. Nonetheless, many Galactic satellites do not possess reliable proper motions, and in any case the number of such objects is limited. A further problem is the ambiguous position of the Leo I dwarf satellite, which has a large line of sight velocity and Galactocentric distance (Sohn et al. 2013). Leo I, if included, contributes $\sim 30\%$ to Watkins et al. (2010)’s estimate of the virial mass of the Milky Way. However, there is an element of circularity in this argument, as once Leo I is assumed to be bound, the mass of the Milky Way must be large enough to bind it ($\sim 2 \times 10^{12} M_{\odot}$) !

On smaller scales, the tidal streams emanating from the satellites of the Milky Way have been suggested as useful constraints on the mass. This has been done most memorably by Koposov et al. (2010) in their modelling of the

* E-mail: sljg2,vasily,nwe@ast.cam.ac.uk

GD-1 stellar stream. Note that the GD-1 stream is only ~ 15 kpc from the Galactic centre, so their analysis constrains the mass out to modest Galactocentric distances. What is needed is the modelling of a much more gigantic structure that reaches out to much greater distances.

Recently, Belokurov et al. (2014) have demonstrated that the trailing arm (see e.g. Koposov et al. 2012, 2013; Slater et al. 2013) of the Sagittarius (Sgr) stream can be traced out to its apocentre at ~ 100 kpc. This confirms the earlier discovery of Newberg et al. (2003) and complements the earlier detections of the leading debris, whose apocentre lies at ~ 50 kpc (Belokurov et al. 2006). The vast scale of the Sgr stream has therefore only recently become apparent. It spans an enormous range of Galactocentric radii, unparalleled when compared to other known Milky Way streams and substructures. Thus, the Sgr stream gives us a unique opportunity to make a precision measurement of our Galaxy's mass out ~ 100 kpc, far further than hitherto possible.

However, to carry this out program requires the development of new modelling techniques. In the past, N-body simulations have been fitted to Sgr stream data with some success (e.g. Fellhauer et al. 2006; Law & Majewski 2010), but they suffer from the drawback that they are extremely time-consuming and so preclude a full exploration of parameter space. Other attempts at potential inference using the Sgr stream (e.g. Deg & Widrow 2013; Vera-Ciro & Helmi 2013; Ibata et al. 2013), while typically faster than the full-blown N-body computations, have not tackled the problem of producing realistic looking streams.

The main aim of this paper is to develop an approximate method of quickly generating streams with realistic centroids by stripping stars at the tidal radius of a progenitor. Their evolution in the Galactic gravitational potential gives us the morphology of the stream, and in particular the locations of the apocentres of the leading and trailing branches. This enables us to search through a large class of models to constrain the mass of the Milky Way.

The structure of the paper is as follows. In Section 2, we summarize the data on the Sgr Stream. Section 3 introduces a new way to generate streams and thence to perform inference on the Milky Way potential, which we term modified Lagrange Cloud Stripping (mLCS). The mLCS algorithm is tested against simulations of disruption in realistic Milky Way-like potentials in Section 4. Finally, in Section 5, we apply this method to the observations of the Sgr Stream to recover an estimate of the mass profile of the Milky Way. Section 6 summarises our results and their implications for conundrums such as the “Too Big To Fail Problem”.

2 THE DATA

The most direct way of inferring the Galactic gravitational potential is by modeling the paths of test particles orbiting in it. Such inference, however, suffers from degeneracies if only a small section of a single orbit is observed (see e.g. Eyre & Binney 2009). In spherical potentials, the rosette pattern of an orbit can be uniquely described by the size and eccentricity of its “petals” – or equivalently the apocentric and pericentric distances and the azimuthal precession rate (see e.g. Binney & Tremaine 2008).

In the Milky Way, of all known stellar tidal streams,

Table 1. The Sagittarius dwarf at a glance

Property	Value	Ref
Galactic latitude b	$-14^\circ.1669$	[1]
Galactic longitude l	$5^\circ.5689$	[1]
Heliocentric distance d_\odot	22.0 to 28.4 kpc	[2]
Heliocentric LOS velocity $v_{r\odot}$	$153 \pm 2 \text{ km s}^{-1}$	[3]
Proper motion μ_b	$1.97 \pm 0.3 \text{ mas yr}^{-1}$	[4]+[5]
Proper motion $\mu_l \cos b$	$-2.44 \pm 0.3 \text{ mas yr}^{-1}$	[4]+[5]
[1] Majewski et al. (2003)		[2] Kunder & Chaboyer (2009)
[3] Ibata et al. (1994)		[4] Pryor et al. (2010)
[5] Dinescu et al. (2005)		

only the Sgr stream has data covering two nearly complete orbital loops, one for the leading tail and one for the trailing. As Belokurov et al. (2014) show, the apocentre of the leading tail is firmly placed at ~ 50 kpc and the trailing debris are revealed to reach the maximal distance of ~ 100 kpc from the Galactic centre. The opening angle, as viewed from the centre of the Galaxy, between the positions of the respective apocentres is measured to be $\sim 93^\circ$. The apocentric distances of the two tails contain information on the extent of the progenitor's orbit. Importantly, these also reflect the differences in energy and angular momentum between the orbit and the debris, which is essential for the stream modelling. The differential precession is controlled, to first order, by the radial mass profile in the Galaxy, but also is a weak function of the Sgr's orbital eccentricity. Finally, to complete the model, we require the location of the progenitor in both position and velocity space. These values will be taken from the literature. In essence, to measure the total mass distribution in the Galaxy, we aim to reproduce the apocentric distances together with the differential precession angle ($r_{aL}, r_{aT}, \Delta\psi$) of the Sgr stream.

Our best knowledge of the Sgr's current position and velocity is summarised in Table 1. Where there is disagreement in the literature as to the value of some of these properties, we have tried to be as conservative as possible. This is especially evident in the determination of the heliocentric distance (see Kunder & Chaboyer 2009, for a summary of recent measurements), which we assume lies somewhere between the extrema of values measured (22.0 - 28.4 kpc). The two best estimates of the progenitor's proper motion (Dinescu et al. 2005; Pryor et al. 2010) agree reasonably well with one another, so we take the mean of their determinations as a best estimate.

We take care in converting from the observable space of heliocentric distance and proper motions to the true Galactocentric distance and velocities to avoid introducing any biases. For the peculiar motion of the Sun with respect to the Local Standard of Rest (LSR), we take $(U, V, W) = (11.1, 12.24, 7.25) \text{ km s}^{-1}$ from Schönrich et al. (2010). For the distance from the Sun to the Galactic center, we use $R_0 = 8$ kpc and we take the circular speed ¹ at R_0 to be $v_c(R_0) = 237 \text{ km s}^{-1}$.

¹ Note that we do not tie the circular speed at the Solar radius to the fitted halo model as this induces a bias at small Galactocentric radii of the order of 10%.

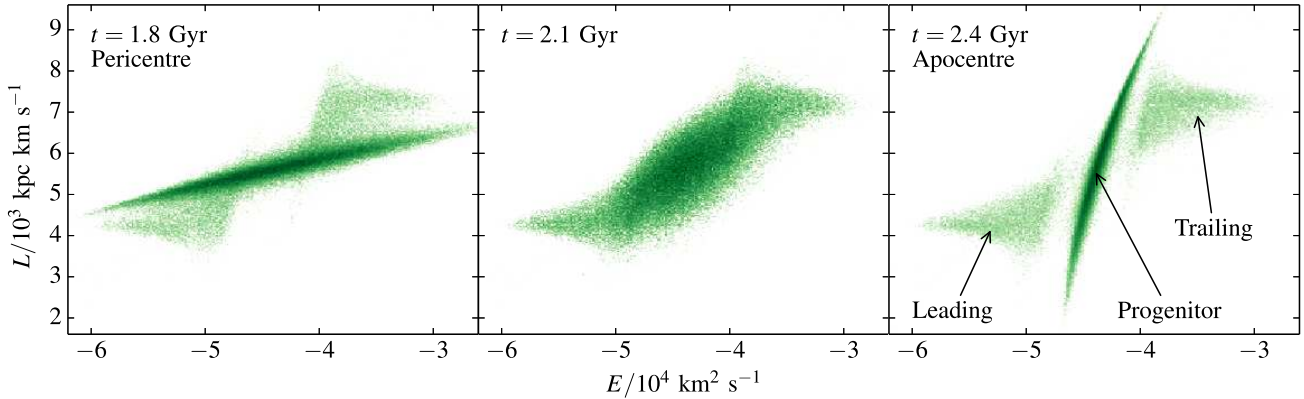


Figure 1. The formation of a tidal stream in the energy and angular momentum space. Each of the three panels show snapshots of an N-body simulation in E and L space at different time steps along the progenitor’s orbit, namely at pericentre (left), between pericentre and apocentre (middle) and at apocentre (right). The progenitor forms an elongated pseudo-ellipse which rotates (and changes its aspect ratio) as the orbital phase of the satellite grows. In this diagram, the unbound debris are seen as two fans offset from the E and L of the progenitor’s centre of mass. The cloud with greater E and L is the trailing arm and the fan with lower E and L is the leading arm. Once unbound the positions of stars in the “bow-tie” are frozen (bar possible small changes of the angular momentum in non-axisymmetric potentials).

3 THE MODEL

Motions of bodies in a gravitational field are deterministic. Thus, in principle, given the full velocity and position information for only 2 points on the orbit, initial and final, the underlying potential can be constrained. This inspires *Rewinder* (Price-Whelan & Johnston 2013), which takes advantage of the fact that the initial conditions for stars in the tidal debris are fully specified if the progenitor is identified and its orbit is known. Similarly, Yu & Madau (2007) show that it might be possible to constrain the Galactic halo triaxiality based on the current positions and velocities of hypervelocity stars, assuming these originate in the vicinity of the central black hole. In reality, we rarely have accurate measurements of all six phase-space coordinates across large distances in the Galaxy. Instead, we typically attempt to leverage the precise knowledge of some of the six dimensions along a length of an orbit to simultaneously infer the initial conditions as well as the properties of the force field.

Stellar streams follow their progenitors’ orbits approximately. That is to say, there exists an offset between the satellite’s orbit and each of the two tidal arms of the stream. Quite simply, the stars in the debris are launched with initial conditions that are slightly different from those of the progenitor. If sphericity of the underlying potential is assumed, then the misalignment between the stream and the orbit can be modelled simply by using the debris energy and angular momentum distributions (e.g. Johnston 1998). In general, this orbit-stream deviation (see e.g. Eyre & Binney 2011) can be stipulated in terms of a change in actions and phases between the progenitor and the tidal debris (e.g. Sanders & Binney 2013). As Eyre & Binney (2011) illustrate, stars bound to the progenitor form an ellipse in action-space, whose flattening and orientation are tied to the orbital phase of the progenitor (see their Figure 10). As the progenitor moves along the orbit and the ellipse rotates, the stripped stars are frozen in action-space in those exact configurations they were at the time of unbinding. As the disruption contin-

ues, the segments of the rotating ellipse contributed by the stripped stars start to overlap, forming a bow-tie pattern. This picture clearly indicates that there is an intricate link between the time of disruption and the orbital parameters of the stripped stars. However, the complexity of the debris properties is largely concealed if the disruption is visualized in frequency space. Here, the leading and the trailing tail distributions look nearly one-dimensional and can be modelled as Gaussian (see e.g. Bovy 2014; Sanders 2014).

Based on the pioneering ideas of Helmi & White (1999), such stream models built in action-angle and frequency space have been shown to work extremely well for cold streams, i.e. those originating from progenitors with masses up to $10^7 - 10^8 M_\odot$ (for discussion, see e.g. Bovy 2014). For more massive systems, the assumption that the distribution of debris in action space can be approximated by a Gaussian and that the frequency offset between the progenitor and the stream is constant throughout the disruption are likely to break down. Additionally, above $10^8 M_\odot$ the gravity of the progenitor is bound to muddle the elegant predictions based on the action-angle formalism. According to Niederste-Ostholt et al. (2010), before the disruption, the progenitor of the Sgr stream had in excess of $10^8 M_\odot$ in stellar mass alone. It is expected that the total mass of the Sgr dwarf was even higher, quite possibly surpassing $10^9 M_\odot$. Therefore, to analyse the properties of the Sgr tidal tails, we strive to build a stream model that works equally well for progenitors of any mass.

3.1 Tidal Stream Mechanics

The objective of this paper is to explore the many-dimensional space spanned by the parameters controlling the mass profile in the Galaxy, while simultaneously fitting for the appropriate progenitor model. Therefore, our method of producing tidal tails must be as fast as possible while maintaining the necessary degree of likeness when compared

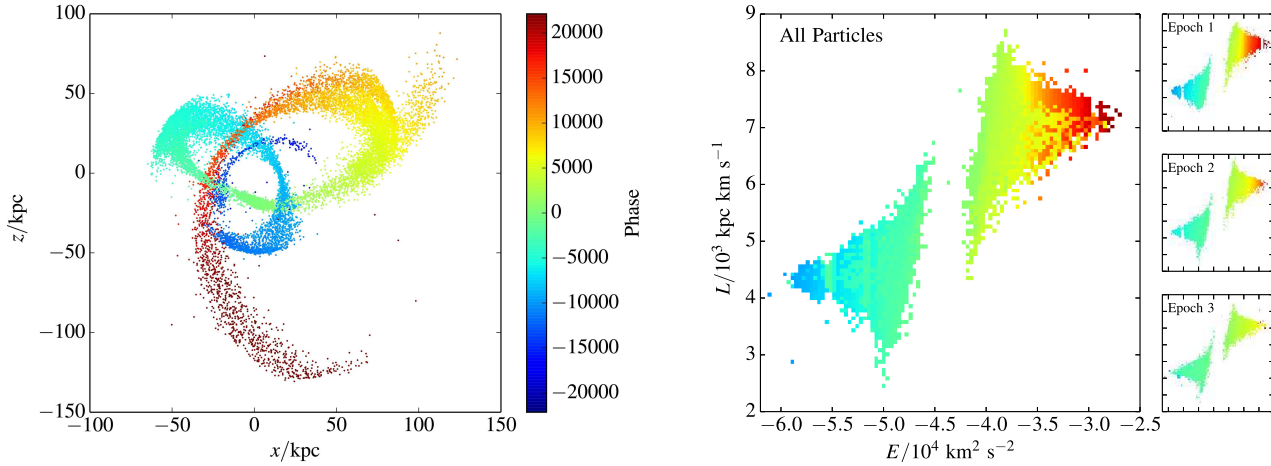


Figure 2. *Left:* Distribution of the tidal debris produced in the N-body simulation in configuration space. The particles are coloured by “phase”, a metric monotonically increasing along the stream. This particular snapshot of the simulation corresponds to the fourth pericentric passage, some 4 Gyr after the onset of disruption. *Right:* Distribution of the debris in E and L space. The colouring scheme applied to the stream “bow-tie” is the same as in the Left panel. The particles are binned in E and L space and the median value of the phase in each bin is shown. The main panel shows all stream particles created up to this time-step. The mini-panels on the right show the distributions of particles created at the previous stripping epochs. Note that particles created the earliest (Epoch 1) have had the most time to spread along the stream, thus creating a strict energy sorting. Even though particles from different individual epochs overlap in the configuration space, the energy sorting persists as evidenced by the main panel.

to a “gold standard” stream. But what would such a gold standard be in the case of the Sgr ?

Given the estimated mass of the dwarf prior to disruption and its orbital period, it seems appropriate to have a “live” (as opposed to a static parameterized density-law) N-body and hydrodynamical model for both the host and the satellite. The need for the inclusion of not only the dark matter, but also gas and stars is dictated by the complexity of the available Sgr stream data. Both leading and trailing tails show strong metallicity gradients and evidence for star formation that possibly ceased only a few Gyrs ago. Moreover, each of the tails seems to be bifurcated into a bright and faint component (Belokurov et al. 2006; Koposov et al. 2012). The very few studies that address the problem of the disruption of a system with multiple components do find that it can affect the resulting tidal tails significantly (see e.g. Peñarrubia et al. 2010; Niederste-Ostholt et al. 2012). Similarly, there are many reasons for the Milky Way model itself to be “live”. First, this would naturally account for the dynamical friction effects. Second, the Sgr disruption could have been going on for so long (see e.g. Fellhauer et al. 2006) that the Galaxy’s mass distribution has evolved. Finally, not all combinations of the disc and the dark halo that can be written down in a parameterized form are actually stable. However, as Debattista et al. (2013) show, in a “live” Milky Way the disc and the central parts of the halo would adjust to each other’s presence to form a long-lived configuration.

As far as we are aware, such an in-depth study of the Sgr disruption does not yet exist. Instead, the most widely cited recent analysis (Law & Majewski 2010) relies on N-body modelling in which the host potential is parameterized (and fixed), while the single-component satellite is represented with particles. While not the ideal specification, this particular simulation does reproduce the largest number of observables in both the progenitor and the stream to date.

Thus, we attempt to build a rapid modelling algorithm that reproduces the salient features of tidal streams produced in N-body simulations such as that of Law & Majewski (2010). Our goal, however, is to speed the stream production by several orders of magnitude.

Before we proceed to assemble the stream model, let us have a glance at a typical satellite disruption. The progenitor’s evolution in the external gravitational potential is simply understood in the action-angle and frequency space, but it is equally transparent when looked at in energy and angular momentum (E , L) space. Fig. 1 shows the results of the simulation of the disruption of a satellite modelled as a Plummer sphere with $6.4 \times 10^8 M_\odot$ and $a = 0.85$ kpc in a spherical NFW potential (Navarro et al. 1996) with the mass $7.5 \times 10^{11} M_\odot$ and the concentration $c = 20$. The satellite is represented with 10^5 particles and the optimal smoothing length was chosen according to the prescription of Dehnen (2001). The orbit has apocentre at 70 kpc and pericentre at 18 kpc and was evolved for 4.31 Gyr (~ 3.5 orbital periods). These choices of parameters for the satellite and its orbit are chosen to mimic those of the Sgr dwarf. The satellite disruption simulation was carried out using the Gadget-2 code (Springel 2005). This utilises a tree algorithm to calculate the forces between each of the particles in the simulation. We have modified the code to implement a static Milky Way potential by adding an additional force component, dependent on position, at each force computation.

Note that the projection of the progenitor’s distribution function onto the (E , L) space forms a shape closely resembling an ellipse. The inclination of the ellipse can be approximated using the expressions for particle excursions in (E , L) space presented in Equation 10 of Yoon et al. (2011). For Roche lobe under-filling satellites and satellites with small Roche lobes, the terms with ΔR can be neglected, giving

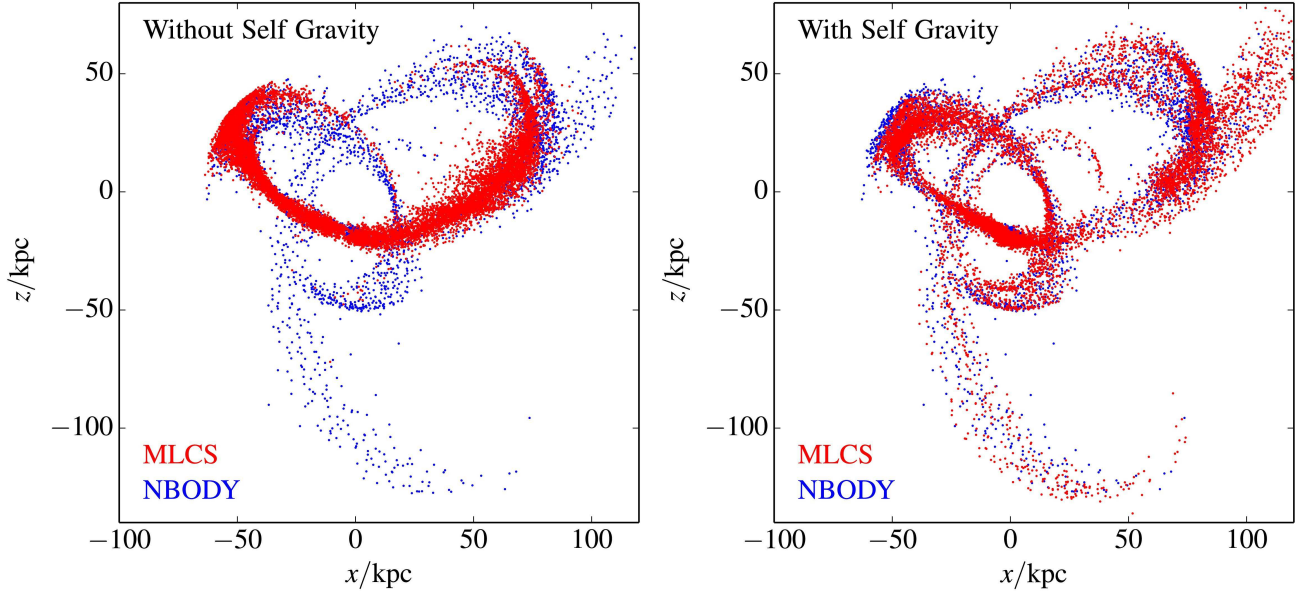


Figure 3. Comparison between the N-body simulation (blue) and the Modified Lagrange Cloud Stripping method (red), excluding (left) and including (right) the effects of the progenitor’s gravity. The snapshot shown is at 4.31 Gyr after the start of the simulation, just after the progenitor’s 4th pericentre passage. It is evident that the inclusion of the progenitor’s gravity is required to correctly model warm streams. If the progenitor’s gravity is not included, the model stream barely reaches half of the length of the N-body representation.

a simple expression for the ratio of the amplitudes of the energy and the angular momentum variations:

$$\frac{\Delta E}{\Delta L} \simeq \frac{v_p}{R_p}, \quad (1)$$

where v_p and R_p are the current velocity and the Galactocentric distance of the progenitor. The subsequent transformation of the particle distribution happens in the manner identical to the action-space evolution described earlier. As the pseudo-ellipse rotates, the stripped particles “freeze-out” and stop moving within this space. In Fig. 1, these can be seen best in the right panel (which presents the situation at the apocentre crossing) where the debris form two fans, offset from the energy and angular momentum of the progenitor. The leading tail is composed of particles with lower E and lower L , the trailing tail particles have higher E and higher L relative to the progenitor. Curiously, given the shape and the extent of the tidal debris cloud, it barely overlaps with the progenitor’s ellipse at the pericentre and the apocentre. Therefore, one would conclude that very little material is stripped at the pericentric crossing, and almost none at the apocentric.

As Fig. 1 illustrates, there is a tight correlation between the initial conditions of the debris and the orbital phase of the progenitor at stripping. In other words, after just one radial period, the stars in the stream will be sorted according to their energy, with the most distant portions of the tails populated by stars with the largest differences in energy with respect to the progenitor. As the satellite completes the subsequent revolutions on its orbit, the stars in the freshly unbound debris are launched with the same (E, L) properties as the previously torn-off stars, but from locations much

closer to the progenitor as compared to the current positions of the earlier stripped material. Therefore, as the disruption progresses and more stars are being pumped into the tails, the strict energy sorting is blurred: at each location along the stream, the debris possess a mixture of ΔE and ΔL . However, depending on the mass of the progenitor, which determines the extent of the ΔE , ΔL distributions and its orbital period, the debris might not have enough time to fully mix.

Fig. 2 shows exactly how much mixing can be expected for a Sgr-like disruption. The left panel of the Figure shows the distribution of the debris in the orbital plane, color-coded according to the particle offset from the progenitor as measured along the stream. The right panel shows the familiar “bow-tie” pattern of debris in (E, L) space color-coded using the same notation. This particular snapshot of the simulation corresponds to the fourth pericentric passage, some 4 Gyr after the onset of disruption. Up to now, the satellite has experienced 3 bouts of tidal stripping and the extent of the debris unbound in each round can be gleaned from the three mini-panels accompanying the right panel of the Figure. These show the obvious: stars stripped as recently as 1 period ago, (i.e. Epoch 3) have not had much time to travel far enough along the stream. On the other hand, the stars stripped in the very beginning of the disruption (Epoch 1) now cover the entire extent of the tidal tails. Note however, that notwithstanding the apparent mixing, at each location along the stream, the superposition of the debris stripped at different times remains ordered in energy space.

3.2 Modified Lagrange Cloud Stripping

Naturally, any stream model aiming to closely reproduce the results of an N-body simulation like the one discussed above must be able to generate the tidal debris with the correct shape and extent in energy and angular momentum space. However, this condition is only necessary but not sufficient, as the stripped stars must also exhibit a certain amount of correlation between the angle along the stream and $(\Delta E, \Delta L)$. These conditions are straightforwardly realised within the framework outlined by Varghese et al. (2011) and Küpper et al. (2012) where particles are released from the two Lagrange points around the progenitor as it moves in the galactic potential. Here, we utilise a subtly different method as – rather than predicting the centroid of the stream directly – we instead generate individual stream members. It is from these members that we calculate the track of the stream and the location of the apocentres to compare with the observed data. This is very similar to the methodology used by Lane et al. (2012) in their modelling of the tidal tails of 47-Tuc, here we will demonstrate the method’s utility in producing streams from progenitors 1000 times more massive. Let us first explain how the method works in practice and then prove that it passes the necessary quality checks.

We start by taking the current position of the progenitor and integrating it back in time in the assumed galactic potential, Φ , to its position at a time $t = -t_{\text{back}}$ from the present day. Stream particles are then produced at equal time steps δt along the orbit of the progenitor from $t = -t_{\text{back}}$ to the present day. These are launched from two locations on the line joining the progenitor to the galactic centre at radial offsets $\Delta r = \pm r_t$, where r_t is the instantaneous tidal radius of the progenitor defined by:

$$r_t = \left(\frac{GM_{\text{sat}}}{\Omega^2 - \frac{d^2\Phi}{dr^2}} \right)^{1/3} \quad (2)$$

Here M_{sat} is the mass of the progenitor and Ω is the instantaneous orbital angular velocity of the progenitor. The particles released closer to the Galactic centre ($\Delta r < 0$) will form the leading arm of the stream and the particles set free further away from the Galactic centre ($\Delta r > 0$) will form the trailing arm. The velocity of these particles are drawn from a Gaussian distribution centered upon the velocity of the progenitor with a dispersion σ in each direction. This dispersion is chosen to be representative of the internal velocity distribution of the stars within the outer parts of the progenitor. The clouds of stream particles released at Lagrange points are then evolved within the combined potential of the host galaxy and the progenitor until the present day ($t = 0$). In our experiments, the progenitor’s potential is treated as a Plummer sphere of fixed mass M_{sat} and scale radius a_{sat} which moves along the orbit of the progenitor.

Each of the created particles are entirely independent of one other (since the progenitor’s orbit is determined only by the galactic potential) therefore will scale linearly with the number of particles produced. Thus each particle can be evolve separately using an adaptive stepping algorithm, naturally accounting for the differences in dynamical times between the particles which are recaptured by the progenitor and those which quickly escape. Whilst this would imply that the mLCS algorithm is trivially parallelizable, we opt

not to, instead using a parallelizable MCMC sampler when exploring parameter space.

Our model requires 3 hidden parameters to describe the structure of the progenitor: its mass M_{sat} , an internal scale length a_{sat} , and the velocity dispersion in the outer parts of the progenitor σ . Note that, while in principle one should be able to calculate the third from any two of these for a self-gravitating body, we opt to keep all three independent. This is due to the fact that the progenitor of the Sgr Stream was presumably embedded in a dark matter halo as it was accreted, and this will affect the velocity dispersion of the satellite’s stars especially in the outer regions. The degree of this embeddedness is unknown and therefore to encode our ignorance we leave all three parameters within the model to be marginalised over. Note that, additionally, Küpper et al. (2012) require a special treatment of the tangential component of stream velocity: having experimented with values between the orbital and the angular velocity of the progenitor, the settle on the latter. We find this distinction makes no perceptible difference to the model streams that we produce and therefore we stipulate, for simplicity, that the debris mean velocity for both leading and trailing tails is that of the progenitor.

One crucial difference between our stream model and the previous implementations based on Modified Lagrange Cloud Stripping is the inclusion of the progenitor’s gravity. Fig. 3 compares a stream produced in N-body simulation (blue points) and two different runs of our model (red points), without (left) and with (right) the progenitor’s gravity. Without the effects of the satellite’s gravity, the tidal tails seem to possess approximately the correct shape, but drastically reduced length. This paper is concerned with the modelling of the positions of the Sgr leading and trailing apocentres. However, having such stubby tails means that the apocentres would be barely reached by the stream particles, therefore biasing the model prediction. The right panel of Fig. 3 and Fig. 5 demonstrates that the inclusion of the satellite’s potential produces a tidal stream almost indistinguishable from the N-body realization in configuration and velocity spaces as well as reproducing the overall structure of the stream in integral of motion space (albeit with a distribution which is slightly more extended in energy space than the N-body). The slight differences appear mostly in the density of stream particles, which we do not expect to be able to reproduce due to the assumption of uniform stripping along the orbit. However, as we shall see in section 4, these minute deviations do not introduce any significant biases when inferring the galaxy’s mass distribution.

Yet, there is one important distinction: the Gadget-2 run took 17.6 CPU hours (i.e. 2.2 hours wall time on 8 cores), producing 31765 particles which were unbound from the progenitor and became members of the stream; on average, this is 2 CPU-seconds per stream particle. Our Modified Lagrange Cloud Stripping model only takes 16 CPU *seconds* to run on a single core of the same server used for the N-body. Here, 12660 particles were created, of which 9022 ended as stream members. This is 0.002 CPU seconds per stream particle. Hence our model shows itself to be 3 orders of magnitude faster than an N-Body to produce the same number of unbound stream particles. This speed increase is primarily due to the fact that we do not attempt to resolve the progenitor with live particles, hence both largely

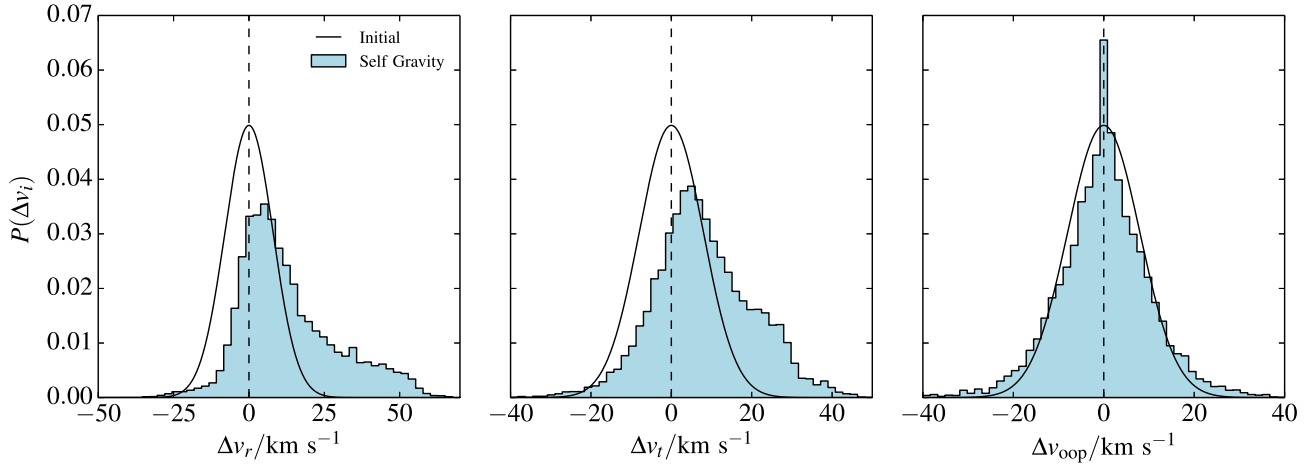


Figure 4. Distributions of the velocity components of the trailing debris particles at the moment of unbinding. The velocity is computed in the frame comoving with the progenitor. The panels show the component of velocity along the line joining the Galactic centre to the progenitor Δv_r (left), the component of velocity orthogonal to this in the plane of the progenitor’s orbit, oriented in the direction of motion of the progenitor, Δv_t (middle), and the component of velocity out of the plane of the progenitor’s orbit, Δv_{oop} (right). Plotted in black is the Gaussian distribution from which velocities of stream particles are initially drawn. The velocity distribution of stream particles the last time they are at one tidal radii from the progenitor is shown by the blue histogram. Note that under the action of the satellite’s gravity, the distributions of velocities become skewed towards higher Δv_t and Δv_r , whilst the component of velocity out of the progenitor’s orbital plane is unaffected.

reducing the number of particles that need to be followed, as well as cutting down the expense of the inter-particle force computations. In both cases the code was run on a dual socket server using quad core Intel Xeon X5460 processors, the GADGET-2 run was parallelized to use all 8 cores whilst the mLCS code ran on only one. Note that the timings presented are for the production of a *single* stream and not for a parameter search. Finally it should also be noted that the speed up of this technique over the N-body run will be dependent on the size, mass and orbit of the progenitor; the timings presented here are for a progenitor that is typical of a Sgr-like object, but could differ e.g. for the case of a much larger plummer sphere the majority of the particles would become unbound almost immediately.

In the next section, we take a closer look at the effects of the progenitor’s gravity which appears to increase the numbers of particles escaping onto orbits with greater ΔE and ΔL as compared to the progenitor itself.

3.3 Action of the Progenitor’s Gravity

Even though the method laid down in the previous Section appears to be an over-simplified brute-force imitation of the tidal disruption process, something curious happens to the clouds of particles released at the inner and the outer Lagrange points in the presence of the progenitor’s gravity. Fig. 4 compares the Gaussian distributions, from which the particle velocities were drawn, with the actual velocity distributions at the time they became unbound from the satellite. The exact unbinding time is not easy to calculate, therefore instead we use the time of the last tidal radius crossing. Fig. 4 shows the distributions of the three velocity components of the trailing tail particles. The chosen projections are: the component of the velocity along the radial

vector v_r ; the component perpendicular to v_r in the plane of the orbit, pointing in the direction of motion of the progenitor, v_t ; and, finally, the component pointing out of the orbital plane v_{oop} . As Fig. 4 illustrates, the leaving population has a prominent excess in v_r and v_t .

With this in mind, it is now easy to explain the discrepancy identified in the previous Section, namely the production of very short tidal tails in the absence of the progenitor’s gravity. The bottom right panel of Fig. 5 gives the E and L distribution of particles produced both with (red) and without (green) the satellite’s gravity. It is immediately obvious that in the case without gravity, stream particles are not launched with sufficiently high energies and angular momenta relative to the progenitor. Thus, the effect of the satellite’s self-gravity is to modify the crude Gaussian approximation of the velocity distribution at the time of stripping to a more realistic one. The initial speeds of the particles drawn from the Gaussian are too low, therefore many of these are accreted by the progenitor. These recaptured particles are then evolved internally within the progenitor until the conditions are favorable for their release. The released particles have an excess in the radial velocity component as they must be traveling away from the satellite. The excess of angular momentum is attained by higher tangential velocities relative to the satellite.

The action of progenitor’s gravity explains why, unlike Küpper et al. (2012), we do not need to tweak the tangential velocity of the released particles. Our stream production works effectively as a constrained N-body simulation where we follow the orbital evolution of large number of massless tracer particles. However, importantly, these are not necessarily stripped at the time at which they are produced within the model. Thus, the absolute distribution of velocities given to stream particles will be erased due to some amount of evo-

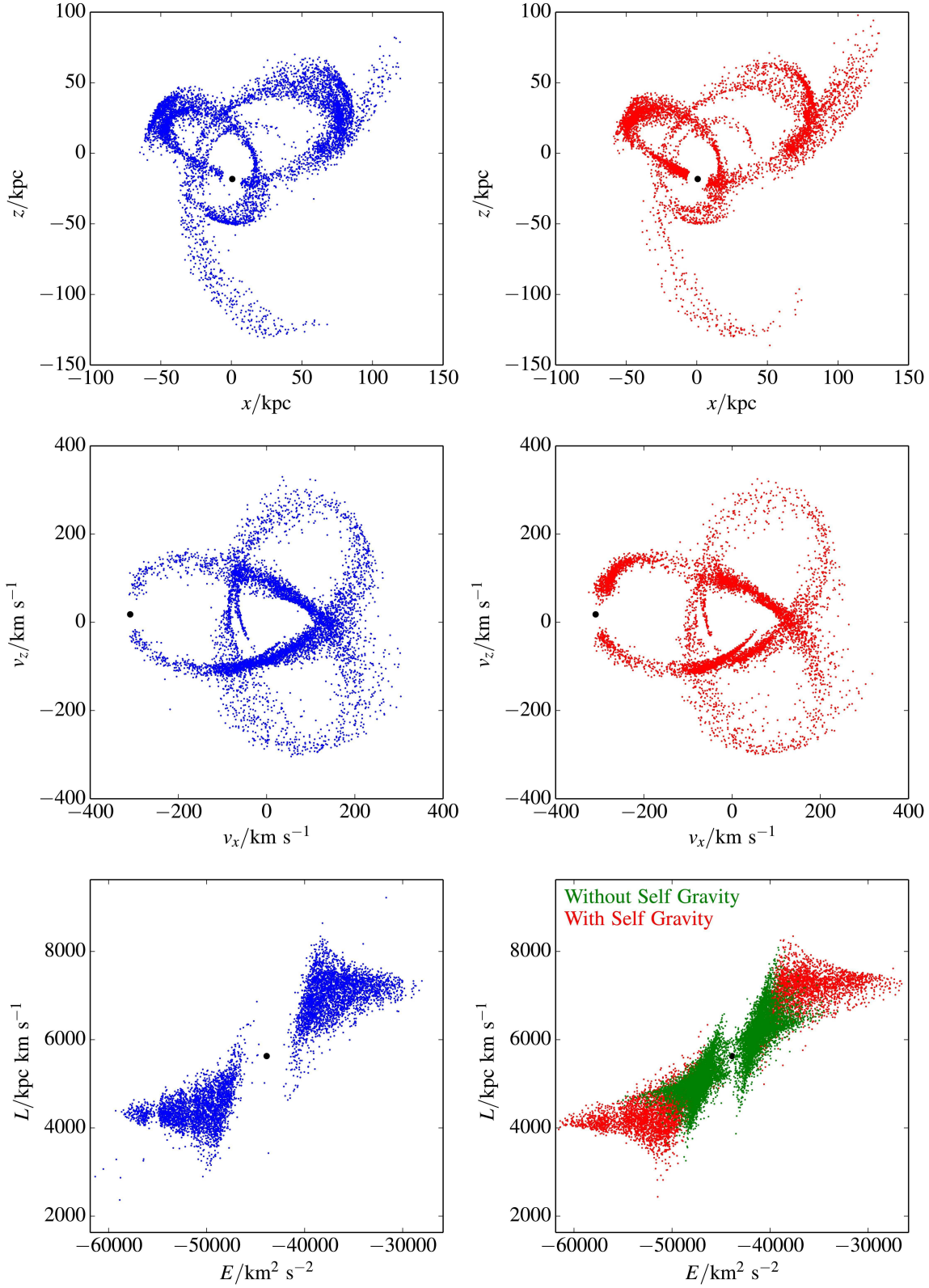


Figure 5. Comparison between an N-body stream (left) and the Modified Lagrange Cloud Stripping model (right) in configuration space (upper), velocity space (middle) and (E, L) space (lower). The location of the progenitor is marked with the black filled circle. For ease of comparison we have plotted a random selection of the N-body particles so that the same number (6500) are plotted for both cases. The bottom right panel also shows over-plotted with green points the energy and angular momentum distribution of the debris in absence of the progenitor's gravity. It is evident that the progenitor's gravity is required to assign the correct orbital properties to the debris particles

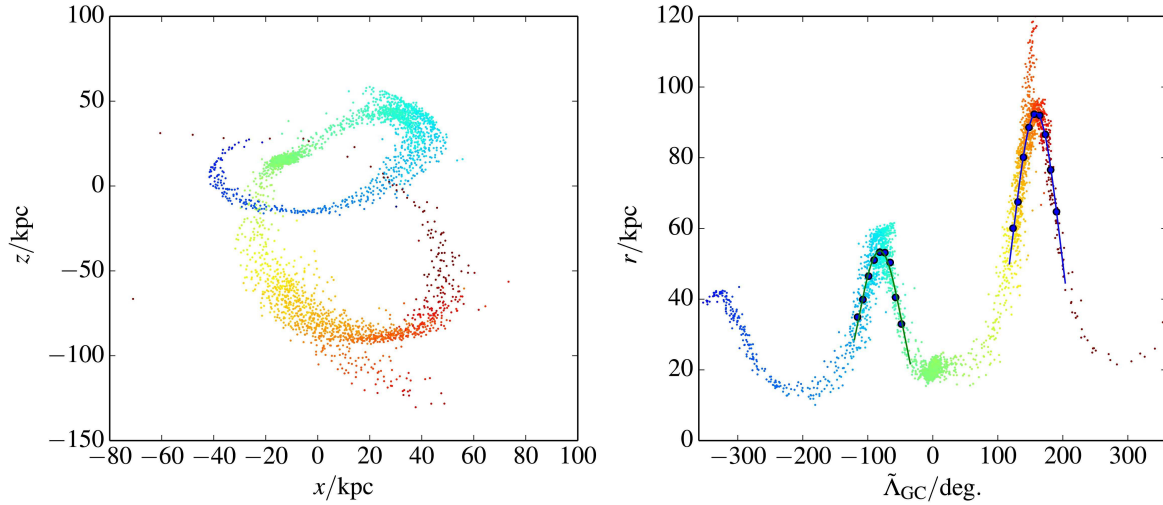


Figure 6. Illustration of the stream unwrapping process and the extraction of the observables. *Left:* This shows the model stream as in Fig. 5 coloured according to the “phase” of the debris. The “phase” metric increases approximately monotonically along the stream. *Right:* This shows the same stream unwrapped as a function of angle (on the celestial sphere) along the stream, measured from the galactic centre $\tilde{\Lambda}_{GC}$ with the progenitor located at $\tilde{\Lambda}_{GC} = 0$. This angle is as defined in Belokurov et al. (2014). The points indicate the centres of the bins used to locate the apocentres and the lines show the fitted Gaussians. This allows to measure the apocentric distances of the mock stream $r_{aL} = 53.6$ kpc and $r_{aT} = 92.6$ kpc as well as the precession angle $\Delta\psi = 119^\circ.5$

lution within the progenitor’s potential. Bear in mind that some accreted particles are never released. We have estimated that the fraction of these stuck tracers is mostly of order of 25% and never above 50%, thus the method can be potentially sped up, but only up to a factor of 2.

The obvious advantage of this stream model is that it should work equally well and equally fast in any host potential, including a live potential, generated, for example, as part of the cosmological zoom-in simulation. However, it should be noted that due to the release of the stream particles at equal times along the progenitor’s orbit, our method will not be able to reproduce the density of stars along the stream exactly. Despite this, stream particles are located where they should be in both the configuration and the velocity space.

3.4 Extraction of Apocentres

We now devise a method to extract the locations of the stream apocentres from the generated particle distributions. The model streams generally have multiple wraps and thus overlap in space. We cannot therefore simply use a simple angular coordinate in the orbital plane to parameterise the location of a particle along the stream. Instead, we construct a method of explicitly unwrapping the stream by defining a coordinate which increases monotonically along the stream.

To do this, we introduce the phase (χ) of each particle, which is defined as follows:

$$\chi = \sum \sqrt{x^2 + y^2 + z^2} - \sqrt{x_p^2 + y_p^2 + z_p^2}. \quad (3)$$

Here, the sum is taken over equal time steps for each stream particle, from the moment that it is generated in the model up until the epoch of observation. The subscript p’s

denote the progenitor. This definition works as the particles in the leading (trailing) arm tend to be at positions which have lower (higher) Galactocentric radii than the progenitor. Whilst this doesn’t provide an entirely monotonically increasing variable, it does work well enough for our purposes to unwrap the stream particles and to identify how each segment of the stream joins together. The results of applying this method are demonstrated in Figs 2 and 6.

With the model stream unwrapped, we can measure the centroids of the apocentres along each of the dimensions of the phase-space. This is done in a manner which is as close as possible to the method used in analysing the observational data (Belokurov et al. 2014). In general, more than one apocentre of the stream is produced with this method (and would be produced in reality as the stream lengthens with time). The data presented in Belokurov et al. (2014) are almost certainly from the first wrap of the stream, and thus we consider only the closest apocentre to the progenitor for both the leading and trailing arms. The trailing arm can show a feature in which the debris stripped from the most recent orbital passage lies on top of the measured apocentre of interest and must therefore be removed from the apocentre detection (see the right hand panel of Fig. 6). This can be done by removing any particles stripped between the last apocentric passage of the progenitor and the current epoch, where we define the stripping time to be the last time that the stream particle was within r_t of the progenitor. Next, we bin the stream particles as a function of angle along the stream to produce an estimate of the stream’s centroid. With this estimate, we then find a first approximation to the positions of the apocentres as the bins showing a local maximum closest to the location of the progenitor. We then take the stream particles within $\pm 40^\circ$ of the initial guess, and fit a

Gaussian to the binned particles in this range². An example of this binning and the extraction is shown in the right hand panel of Fig. 6.

3.5 Galactic Potential Model

The final ingredient required to carry out the inference is the model for the Galactic gravitational potential. The HI rotation curve in the inner Milky Way is flat to a good approximation. Once the HI gas gives out beyond ~ 20 kpc (e.g. Sofue et al. 2009), the rotation curve may continue flat or may decline. A simple yet flexible family of models which encompasses such behaviour is:

$$v_{\text{circ}}^2 = \frac{v_0^2 r_s^\alpha}{(r_s^2 + r^2)^{\alpha/2}}. \quad (4)$$

The implied Galactic density is

$$\rho(r) = \frac{v_0^2 r_s^\alpha}{4\pi G r^2} \frac{r_s^2 + (1 - \alpha)r^2}{(r_s^2 + r^2)^{1+\alpha/2}}. \quad (5)$$

Naturally, given the sphericity of these models, the enclosed mass as a function of radius can be found directly from v_{circ} :

$$M(r) = \frac{r v_{\text{circ}}^2}{G} = \frac{r v_0^2 r_s^\alpha}{G (r_s^2 + r^2)^{\alpha/2}}. \quad (6)$$

We shall refer to these models as the truncated, flat rotation curve family (TF). The circular velocity curve (4) is flat with amplitude v_0 in the inner parts and tends to a power-law with slope $-\alpha/2$ in the outer parts with the transition scale given by r_s . A plot showing the variety of possible rotation curves is shown in Fig. 7. When $\alpha = 0$, this is the singular isothermal sphere. When $\alpha = 1$, this is the model first introduced by Lin & Lynden-Bell (1982) to study the orbits of the Magellanic Clouds and subsequently used by Wilkinson & Evans (1999) in their measurement of the mass of the Milky Way. As $0 \leq \alpha \leq 1$, the outer rotation curve spans the physical range from flat to Keplerian. Note, that our model represents the combined contribution of the disc and the dark halo to the rotation curve. On the plus side, it is extremely concise, but it suffers from the obvious drawbacks: it is spherically symmetric and does not contain a mass component mimicking the central over-density due to the Galactic bulge/bar. Nonetheless, surprisingly, as we demonstrate in Section 4, this simple model does not suffer any significant biases when applied to analyze the behaviour of streams produced in significantly more complex potentials.

It is illuminating to enquire how sensitive the predicted observables are to each of the model parameters. We take a progenitor with a fixed position and velocity today and vary each of the parameters in turn whilst keeping the others fixed. The results are shown in Fig. 8. As the rotation curve

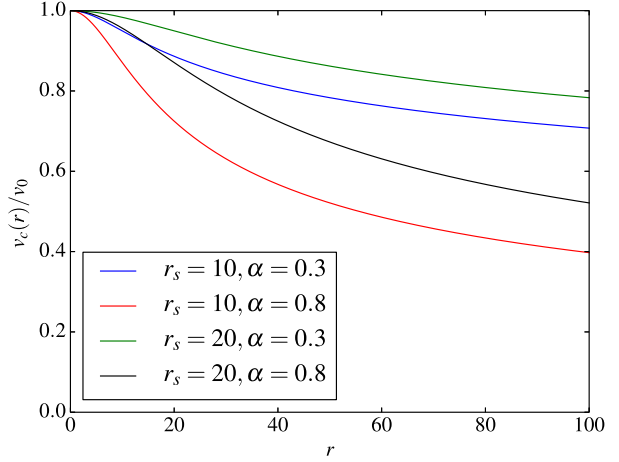


Figure 7. Selection of rotation curves generated by the truncated, flat rotation curve (TF) model. As $\alpha \rightarrow 0$, this corresponds to the everywhere flat rotation curve of an isothermal sphere. As $\alpha \rightarrow 1$ and $r_s \rightarrow 0$, the model tends towards the Keplerian point-mass limit of $v_{\text{circ}} \propto r^{-1/2}$.

becomes more steeply decreasing in the outer parts (r_s decreases and α increases), we see that the precession angle $\Delta\psi$ increases. This is the same qualitative behaviour one would expect by treating the stream as an orbit (Belokurov et al. 2014). Fig. 8 also gives a clear prediction as to how the inter-arm apocentric distance difference behaves: lighter Milky Ways, either due to a smaller circular velocity normalization or due to a steeper fall-off in density, produce tails that differ the most in their apocentric distances.

Additionally, the difference in apocentric distances decreases as the stream is allowed to evolve for a longer time. This can be understood on noting that the stars produced in each of the arms of the stream have a significant spread in energy (see e.g. Fig. 5). The stars with the greatest difference in energy also have the greatest difference in orbital period as compared to the progenitor. Thus, these end up furthest from the progenitor along the stream and form stream apocentres first. As the stream is allowed to evolve for a longer time, particles with a smaller difference in energy, and thus smaller difference in apocentric radii, reach apocentre thus causing the observed effect. A similar effect can be seen when looking at the dependence on the observables on the mass of the progenitor M_{sat} . Here, we see an increase in difference of apocentric distances on the mass of the progenitor. This is caused by the greater difference in energy between the two arms of the stream.

3.6 Constructing the Mass Estimate

With a model in place to predict the apocentric properties of a stream in a given potential, it is now viable to use the observations to infer the parameters controlling the Galactic mass distribution. This is done by comparing the predictions

² Whilst any strongly peaked function will work adequately here, the choice of a Gaussian is to follow Belokurov et al. (2014) as closely as possible in extracting the observables, therefore circumventing any additional biases introduced by the choice of functional form.

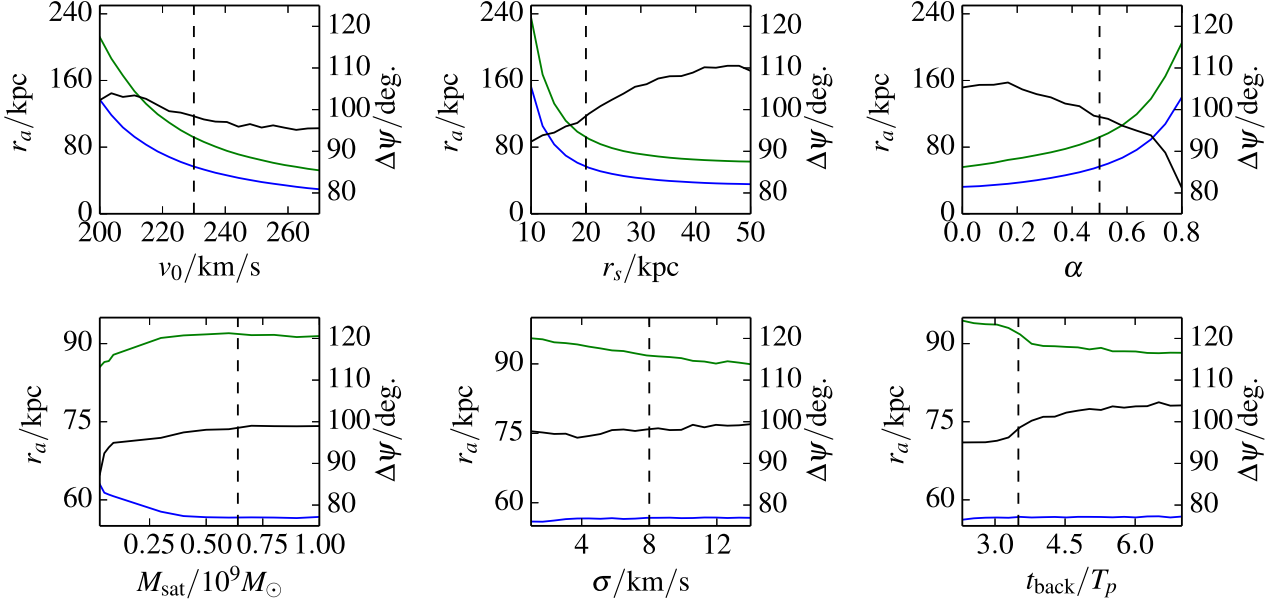


Figure 8. Dependence of each of the observables on one of the model parameters whilst keeping the rest fixed. The blue (green) line shows the apocentric distance of the leading (trailing) tail r_{aL} (r_{aT}), while the black line displays the evolution of the value of differential orbital precession $\Delta\psi$. In each panel, vertical dashed line shows the value that each of the parameters is fixed to when others are varied. Note that the observables are mostly sensitive to changes in the potential model. For example, decreasing v_0 , r_s and increasing α all lead to a lighter Milky Way, which helps to bring the differential precession down and move the two tidal tails apart. Additionally, smaller and subtler evolution of the observables is displayed when the nuisance parameters such as progenitor’s mass and look-back time are varied.

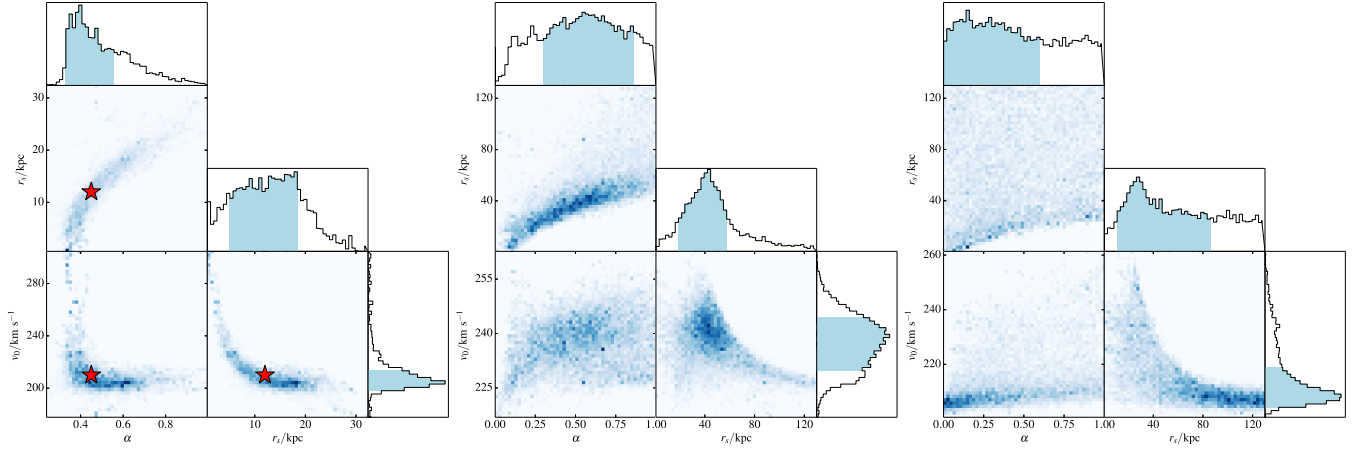


Figure 9. Testing the model on mock stream data. Each of the three groups of panels shows the posterior probability distributions for r_s , α and v_0 when fitting the TF model to the stream observables from the test N-body simulations. *Left Group:* The mock Galaxy is the spherical TF model. While there are obvious degeneracies between the model parameters, the marginalized 1d posterior distributions peak in the close proximity of the input “true” values for α and v_0 marked by red stars. The marginalised posterior for r_s is much broader, nonetheless the input value is well contained within the 68% credible region. *Middle Group:* The mock Galaxy is a three-component model with spherical DM halo. Degeneracies similar to the earlier case are present. However, it is not straightforward to interpret what the peaks in the marginalized posterior distributions symbolize. *Right Group:* The mock Galaxy is that of Law & Majewski (2010). All parameters have long tails in the posterior distributions and evidence for strong degeneracies. However, despite the obvious model mismatch the cumulative mass profiles are closely reproduced (see Fig. 10)

of the model to the observed values with the following likelihood function:

$$\mathcal{L} = \prod_i \frac{1}{\sqrt{2\pi\sigma_i^2}} \exp \left[-\frac{(x_{\text{model},i} - x_{\text{data},i})^2}{2\sigma_i^2} \right] \quad (7)$$

where x_i is each of the observables and σ_i is the error associated with it. The product is taken over each of the three observables, namely the apocentric distances of the leading and trailing arms and the precession angle, $(r_{\text{aL}}, r_{\text{aT}}, \Delta\psi)$

In practice, the model streams are produced by first integrating the Sgr dwarf orbit back from the location in the phase-space which is allowed by the current observations. While all 6 coordinates of the Sgr dwarf have been measured to date, some (for example, the proper motion) carry more uncertainty than the others (for example, location on the sky). This is reflected in Table 1 as well as Table 2 which summarizes the priors used in the modeling. In a nutshell, we are constraining the total of 3 gravitational potential parameters while marginalizing over 10 nuisance parameters in total: 6 controlling the progenitor’s orbital initial conditions, 3 controlling its structural properties, as well as the look-back time

The parameter space is sampled with the parallel Markov Chain Monte Carlo code **emcee** (Foreman-Mackey et al. 2013) to build a set of samples from the posterior distributions. From these, it is a simple task to convert into the estimated mass at a given radius, $M(r)$. We take the joint samples of the potential parameters and calculate the mass implied by each at the radius of interest. By using a large number ($\approx 10^5$) of such samples, we build up the implied posterior on the mass enclosed at a given radius and thus can compute the most likely value and its error with ease.

4 TESTS ON MOCK DATA

To gain confidence in any inferences obtained from our model, we test it for biases using simulations of disruption within a realistic Milky-Way like potential.

4.1 Description of Simulations

The test simulations are performed in three different static Galactic potentials. Our first mock Galaxy is the same as the model used to measure the mass distribution, i.e. the truncated, flat rotation curve family introduced in Section 3.5. The second case is a standard three component model of the Milky Way’s potential with bulge, disc and dark matter halo. Here, the central parts of the potential are flattened due to the disc contribution, but the dark halo and, therefore, the outer Galaxy is spherical. Finally, the third case is the potential proposed by Law & Majewski (2010) with a triaxial dark halo.

In each case, the disrupting progenitor is a Plummer sphere of mass $M_{\text{sat}} = 6.4 \times 10^8 M_\odot$ and scale-length $a_{\text{sat}} = 850$ pc. This yields a satellite with the internal velocity dispersion of $\sim 30 \text{ km s}^{-1}$ in line with observational constraints of the Sgr dwarf. The progenitor was placed on a polar orbit with an apocentre of 75 kpc and a pericentre

of 17 kpc and evolved for ≈ 2.5 orbital periods (~ 3 Gyr) using the Gadget-2 code (Springel 2005).

Using the mock N-body observations, it is possible to test the stream model for any possible biases present in the mass recovery. Of course, the simulation data provide perfect knowledge of the current phase space location of the progenitor. When we apply the model to the real data, uncertainties in the satellite’s coordinates will be marginalised over.

4.2 Truncated, Flat Rotation Curve Model

An N-body simulation of a satellite disruption is carried out in a TF potential with the following parameters. The amplitude of the circular velocity curve is $v_0 = 210 \text{ km/s}$, the scale radius is $r_s = 12 \text{ kpc}$ and the outer power law is $\alpha = 0.45$. The apocentres of the tidal tails were extracted using the method presented in Section 3.4, yielding apocentric radii and a precession angle of $r_{\text{aL}} = 54.6 \pm 1.0 \text{ kpc}$, $r_{\text{aT}} = 90.5 \pm 1.2 \text{ kpc}$ and $\Delta\psi = 85^\circ.8 \pm 1.3$.

The resulting mock stream data are then modeled by applying the mLCS algorithm described in Section 3. In this particular test case, the functional form of the model potential coincides exactly with that used to produce the disruption simulation. The left group of panels in Fig. 9 displays the quality of the inference. Unsurprisingly, there are strong degeneracies between all three model parameters, most prominently between r_s and α . The coupling between the parameters controlling the steepness of the radial mass density profile was already apparent in Fig. 8. Notwithstanding this degeneracy, the true parameter values (marked with red stars) all fall within the uncertainties implied by the posterior distributions.

The accompanying Fig. 10 presents the details of the mass profile recovery. In particular, the left panel shows the results for the mock TF Galaxy discussed here. The true cumulative mass profile is shown in red, while the black curve gives the inferred mass distribution. The slope of the overall mass (dark matter plus baryons) profile changes quickly within 10-30 kpc from the Galactic centre and then stays constant. As is obvious from Fig. 10, the mismatch between the true and the inferred profiles is minimal everywhere within the range considered, i.e. $< 100 \text{ kpc}$. While the systematic error appears tiny, the random error has a characteristic “pinch” radius at around 40 kpc, within which it stays minimal, i.e. 1%, and then blows up to 10% beyond 50 kpc. In other words, the constraining power of the method lies mostly inside the leading tail apocentre (the apocentric distance are marked by vertical dashed lines). Importantly, while the r_s and α parameters are measured with large error-bars due to the above-mentioned degeneracy, the outer slope of the total radial mass profile is clearly constrained, as evidenced by the lack of any significant systematic error between 50 and 100 kpc.

4.3 Bulge, Disc and Spherical Halo

While it is reassuring to see that the model performs well in the case where the functional form of the density and potential distribution is known, we do not have such a luxury when analyzing the real Milky Way. Therefore, we proceed

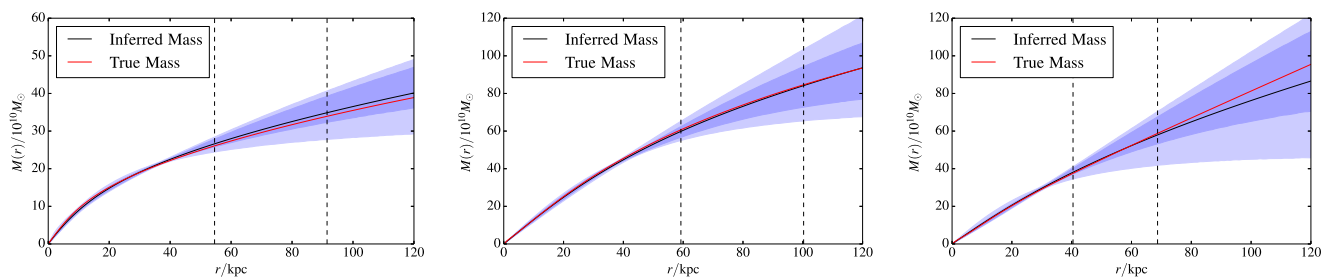


Figure 10. Mass recovery for Sgr disruption in three different mock Galaxies. Red curves show the true cumulative mass profile, while black lines report the most likely model inferences. The dark and light blue regions show the 1 and 2σ confidence regions of the recovered mass. The vertical dashed lines show the radii of the leading and trailing apocentres (with $r_{aL} < r_{aT}$). *Left:* The mock Galaxy is the spherical TF model. Note the “pinch” radius at around 40 kpc where the random error is at its minimum. The systematic offset between the true and recovered mass is less than 1 standard deviation everywhere between 10 and 120 kpc. *Middle:* Cumulative mass profile for the mock three-component Galaxy with a bulge, disc and a spherical dark halo. Results are very similar to the test case shown in the left panel, albeit the random error blows up slightly faster beyond the pinch radius. *Right:* Mass distribution in the mock Milky Way with Law & Majewski (2010) potential. No significant systematic offset between data and the model is detected. Note, however, that beyond 50 kpc, the error regions are the largest of the three cases considered. This is likely to be due to the fact that the stream probes a reduced range of Galactocentric radii in this case as shown by the locations of the apocentres.

to test the algorithm on mock disruption data produced in Galaxies that differ from the assumed model distribution.

Here, in particular, the disruption is produced in the three-component (bulge, disc and dark halo) mock Galaxy, but the stream fitting is done using the TF model. The bulge is taken as a Hernquist (1990) sphere with mass of $M_b = 3 \times 10^{10} M_\odot$ and scale-length $a_b = 500$ pc. The thick and thin discs are represented as a single component which follows the Miyamoto & Nagai (1975) model with total mass $M_d = 3.3 \times 10^{10} M_\odot$, the scale-length $a_d = 4$ kpc and the scale-height $b_d = 400$ pc. Finally, the dark halo is represented with a spherical NFW model (Navarro et al. 1996). The DM halo’s mass is $M_{200} = 1.2 \times 10^{12} M_\odot$ and its concentration is $c_{200} = 16$. The rotation curve given by this three-component model is shown in Fig. 11. It gives a reasonable representation of the LSR as measured by Bovy et al. (2012), with an amplitude of $\approx 240 \text{ km s}^{-1}$ around 8 kpc. The resulting apocentric radii and the precession angle are the following: $r_{aL} = 57.2 \pm 0.6$ kpc, $r_{aT} = 100.3 \pm 0.3$ kpc and $\Delta\psi = 110^\circ.6 \pm 0.7$.

As before, the posterior distributions for r_s , α and v_0 are shown in the middle panels of Fig. 9. Unsurprisingly, the signs of the same degeneracy between r_s and α are clearly visible. It is, however, more difficult to interpret these posterior distributions in view of the mismatch between the input and the model. Nonetheless, regardless of the degeneracy and the model mismatch, the marginalized probability distributions appear to have well-defined peaks. Most importantly, the cumulative mass profile is recovered with inspiring fidelity as evidenced by the middle panel of Fig. 10. As in the previous test case, the posterior distribution of the cumulative mass profile displays a “pinch” at around 40 kpc. Note that the two mock streams actually have similar apocentric distances. The behaviour of the random error beyond 50 kpc is slightly different: it grows to somewhat larger value 13%, which we consider to be symptomatic of the mismatch between the “true” and the assumed Galactic mass distributions. Interestingly, the rotation curve inferred from the stream apocentric data looks a very good match to the input one as seen in Fig. 11.

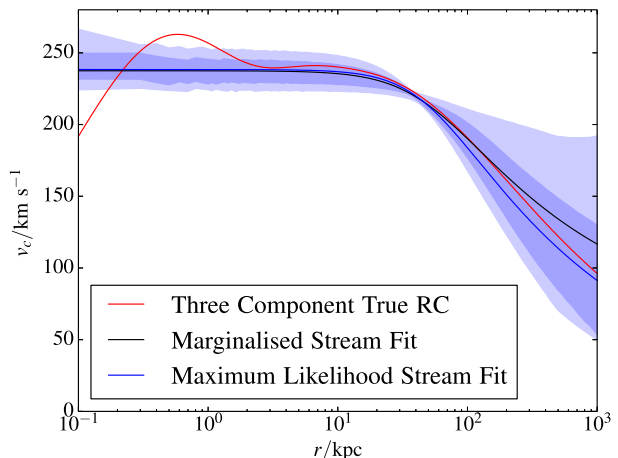


Figure 11. Rotation curve of the three component (bulge, disc and spherical halo) mock Galaxy (red curve). The blue line shows the rotation curve based on the maximum likelihood stream fit, while the black curve is the marginalized stream fit. It is clear that the spherical TF model is a viable choice to describes the mass distribution in a more complex potential in the range of Galactocentric distances probed by the stream (10 kpc - 100 kpc).

4.4 Model of Law & Majewski (2010)

It is clear from the two test cases discussed above that the algorithm can be used to infer the cumulative mass distributions in both spherical and flattened Galaxies. However, how does it cope with a yet more complex potential?

To this end, we produce an N-body simulation of a satellite disruption mirroring the setup of Law & Majewski (2010). The result of their modeling of the Sgr stream data available at the time is intriguing. Together with the usual components for the bulge/bar and the discs, their model favors a DM halo that appears almost perfectly oblate, but with the minor axis stuck in the Galactic plane. The combined gravity of the spherical bulge, highly flattened disc

and the “hockey puck” halo results in a complex overall potential with the shape evolving between 5 and 60 kpc.

The outcome of our N-body simulations looks identical to the snapshots published by Law & Majewski (2010). In particular, for the Sgr stream we find the apocentric radii of following: $r_{aL} = 47.5 \pm 1.3$ kpc, $r_{aT} = 68.7 \pm 1.4$ kpc and the precession angle is $\Delta\psi = 114^\circ.1 \pm 3.0$. Note that these values are markedly different from the early two cases and from those measured as pointed out by Belokurov et al. (2014). The result of applying the model of a stream forming in the TF potential to these mock data are show in the right panel of Fig. 9. The model parameters appear to be even less constrained in this case, although, the marginalized posterior probability distributions for r_s and v_0 do show very clear peaks.

The most important conclusion, however, can be gleaned from the right panel of Fig. 10 which proves that the Galactic total mass and the radial matter distribution can be measured even in such a complicated potential. It is true that both systematic and random error (which is at 20% level at 100 kpc) in this case are larger than the previous two. The “pinch” radius has moved in and is now at around 30 kpc, but this is simply the consequence of the smaller apocentric radii of the mock stream. The mismatch between the true and the inferred mass starts to grow quickly beyond 60 kpc, but stays comfortably within one standard deviation.

5 APPLICATION TO THE MILKY WAY GALAXY

With confidence in our model’s ability to perform unbiased inference, we now turn to the task of fitting the data for the apocentric distances and precession angle of the Sgr stream. The priors used on each of the model parameters are tabulated in Table 2. We use completely uninformed priors on each of the parameters of the Galaxy model, allowing this method to give us an independent measure of the Milky Way’s potential.

The inference on the potential parameters is presented in Fig. 12. Here, the same general structure as with the test cases can be seen, with the obvious degeneracy between r_s and α . In this case, the narrow banana-shaped clouds are significantly broadened due to the noise in the determination of the current phase-space position of the progenitor. The inferred mass profile and rotation curve of the Milky Way are shown in Fig. 13, alongside a selection of recent mass determinations from the literature. According to our model, the cumulative mass profile flattens out at around 40 kpc, and from there onwards remains rather shallow. If the matter density profile actually does not change slope beyond 80-100 kpc, the total Milky Way mass ought to be rather low, i.e. $0.5 - 0.8 \times 10^{12} M_\odot$. Indeed, quantitatively, our measurement appears to be at the lower bound of most previous estimates. We tabulate our mass estimates for a range of radii in Table 3.

At 50 kpc we are in good agreement with the mass determined by Wilkinson & Evans (1999) from satellite and globular cluster motions. There is, however some tension with the measurement from BHB tracers of Deason et al. (2012), where agreement is only at the 2σ level. We are in excellent agreement with the mass measurement out to 60 kpc

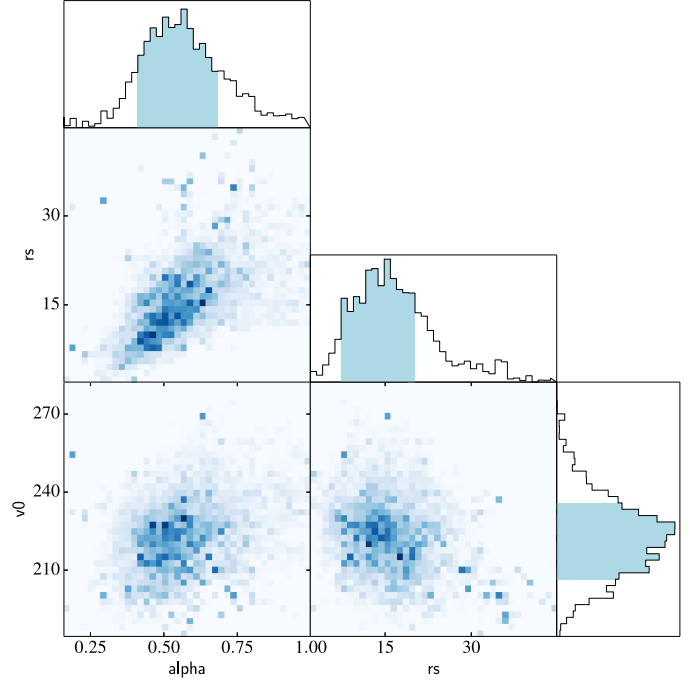


Figure 12. Posterior probability distributions for $r_s - \alpha$ parameters in the TF model as inferred from the Sgr stream precession. Note – as seen previously in the tests with mock Galaxies – that there is a degeneracy between the two shape parameters of the model. However, the degeneracy appears more bloated, most likely due to the uncertainty in the determination of the 6D position of the Sgr dwarf. Histograms show the marginalized posterior for each of the parameters.

of Xue et al. (2008). There is also tension with the measurement of Gnedin et al. (2010) of the mass out to 80 kpc. This discrepancy is easy to explain. The analysis is based on the sample of hyper-velocity stars published by Brown et al. (2010). However, a staggering 50% of these are actually projected to lie in the Sgr stream. The already crippling effects of soaring Sgr stream contamination are possibly exacerbated by additional contamination from Blue Stragglers. A more recent study of the kinematics of the outer stellar halo tracers by Deason et al. (2012) finds evidence of a dramatic drop in the velocity dispersion beyond 50 kpc. Superficially, their measurement of the line-of-sight velocity dispersion beyond 100 kpc, $\sigma_r \sim 60 \text{ km s}^{-1}$ is consistent with our measurement of the circular velocity at similar distances, $V_c \sim 120 \text{ km s}^{-1}$.

Finally, we compare our results to those of Watkins et al. (2010). They performed inference based upon the satellite population of the Milky Way, again assuming smooth density laws. Their results are strongly dependent on the (unknown) velocity anisotropy of their population, giving a wide range of possible masses. They find that the plausible range of masses out to 100 kpc lies between 3.3 and $13.8 \times 10^{11} M_\odot$. The results of this work favour the lower end of their range.

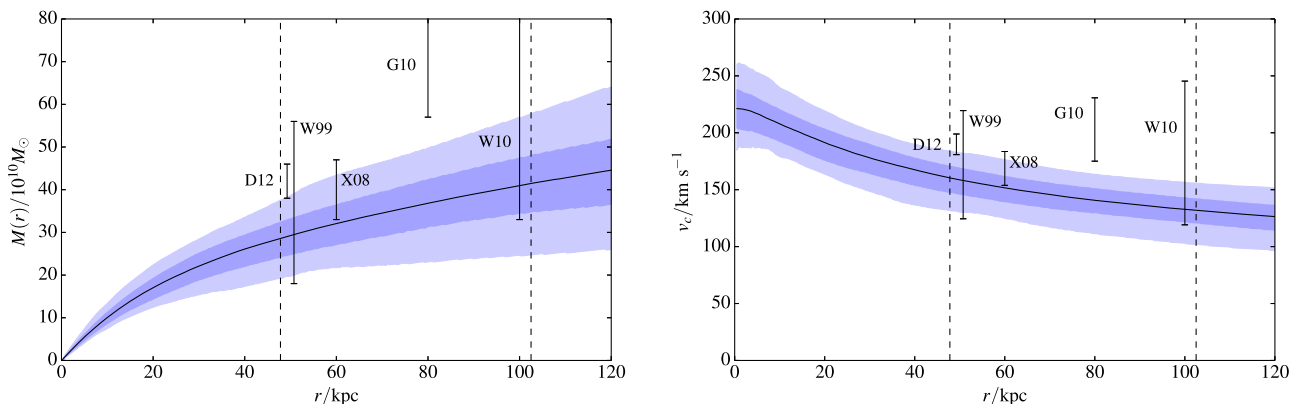


Figure 13. *Left:* Cumulative mass profile of the Milky Way as inferred by the model of the Sgr stream precession. The solid black line shows the most likely mass, the light and dark blue shaded regions show the 68% and the 95% confidence regions respectively. The black points are previous determinations from the literature and are labelled as follows: D12 – Deason et al. (2012); G10 – Gnedin et al. (2010); X08 – Xue et al. (2008); W99 – Wilkinson & Evans (1999); W10 – Watkins et al. (2010). The D12 and W99 points at 50 kpc have been offset from each other for clarity. Note that the error bars for G10 and W10 extend up to $9.9 \times 10^{11} M_{\odot}$ and $13.8 \times 10^{11} M_{\odot}$ respectively. Our mass determination agrees well with most of the literature values, but systematically favors the lower margin of the reported confidence intervals *Right:* Milky Way circular velocity curve as inferred by the model. The solid black line shows the most likely V_c , the light and dark blue shaded regions show the 68% and the 95% confidence regions respectively.

6 DISCUSSION AND CONCLUSIONS

We have developed a rapid algorithm capable to generate realistically looking streams produced in disruption of progenitors of arbitrary mass in arbitrary potentials. In our model, stars are released with a Gaussian velocity distribution at the inner and outer Lagrange points of the disrupting progenitor. An essential ingredient is the inclusion of the effect of the progenitor’s gravity on stream particles around the time of un-binding. In essence, the progenitor’s gravity naturally corrects our crude guess for the velocity distribution of stripped particles to a more realistic one.

This model provides a natural explanation for the differences in the apocentric distances and the precession angle found for the Sagittarius (Sgr) stream in Belokurov et al. (2014). The behaviour of the stream properties is controlled mostly by the host potential in which the satellite is disrupting, though there is a small dependence upon the internal properties of the progenitor. Thus, the observations are explicable without the need to invoke dynamical friction (c.f., Chakrabarti et al. 2014).

Exploiting the sensitivity of the precession measurement to the underlying potential, we tested the ability of our model to infer the potential from mock observations from N-body simulations. We find the model performs remarkably well and produces a nearly unbiased estimate of the enclosed mass. When applied to observations of the precession of the Sgr Stream, we obtain a new measurement of the mass profile of the Milky Way out to distances of ~ 100 kpc. We find the masses within 50 kpc and 100 kpc to be $M(50 \text{ kpc}) = 2.9 \pm 0.5 \times 10^{11} M_{\odot}$ and $M(100 \text{ kpc}) = 4.0 \pm 0.7 \times 10^{11} M_{\odot}$ respectively. We emphasise that this is an entirely independent method to any previous determinations.

What are the limitations of our method? Ideally, when modelling the satellite disruption, one should aim at reproducing the properties of both the stream as well as the rem-

nant. By design, the mLCS algorithm presented in this paper has nothing to say about the final state of the stream progenitor. Additionally, while we have established that the centroids of streams generated by Modified Lagrange Cloud Stripping matches well the centroids of streams produced in N-body simulation, there is no evidence that our model gives realistic density distribution along or the tidal tails. This is because in the current implementation, the stripping rate is independent of time. However, as the N-body simulations show the stellar flux out of the satellite is a strong function of time. Moreover, if the progenitor contains both stars and dark matter, the stellar stripping rate is highly suppressed in the initial throes of accretion, and sharply increases once most of the DM has been removed (see e.g. Niederste-Ostholt et al. 2012). Finally, if the Galactic dark matter halo is strongly triaxial, it might be possible to bias our stream-based inference of the total mass. We have explored how the assumption of sphericity of the overall potential influences the mass recovery. However, none of our mock Galaxies are truly triaxial, for example, the dark halo in the model of Law & Majewski (2010) is nominally triaxial, but in reality it is just a oblate ellipsoid standing on a side.

Our results represent another piece in the growing body of evidence (Battaglia et al. 2005; Bovy et al. 2012; Deason et al. 2012; Rashkov et al. 2013) that suggests the Milky Way galaxy is less massive than previously assumed. The total mass of the Milky Way inferred from the kinematics of satellites depends critically on whether the distant and fast moving dwarf galaxy Leo I is included or not (see e.g., Wilkinson & Evans 1999; Watkins et al. 2010). If Leo I is unbound, then $M(200 \text{ kpc}) \lesssim 1 \times 10^{11} M_{\odot}$, whilst if Leo I is bound, then $M(200 \text{ kpc}) \lesssim 2 \times 10^{12} M_{\odot}$. Boylan-Kolchin et al. (2013) argue that Leo I is most likely bound, as 99.9 per cent of sub-halos in their simulations are bound to the host. Nonetheless, processes to create fast-moving satellites are known. For example, infall of a satel-

Table 2. The priors on each of the model parameters when fitting to the Sgr stream data in section 5. When a uniformly distributed prior is used, the range is indicated with square brackets. When a normally distributed prior is used, the mean and standard deviation is indicated as a pair (μ, σ) in round brackets.

Parameter	Distribution	Prior
Potential Parameters		
v_0	Uniform	[40, 400] km s ⁻¹
r_s	Uniform	[1, 100] kpc
α	Uniform	[0, 1]
Progenitor Properties		
m_{sat}	Uniform	[0.1, 1] $\times 10^9 M_\odot$
a_{sat}	Uniform	[0.1, 1] kpc
σ	Uniform	[0.5, 10.0] km s ⁻¹
Progenitor's Orbit		
l	Fixed	5°.5689
b	Fixed	-14°.1669
d_{helio}	Uniform	[22.0, 28.4] kpc
v_{los}	Normal	(153, 2) km s ⁻¹
$\mu_l \cos b$	Normal	(1.97, 0.3) mas yr ⁻¹
μ_b	Normal	(-2.44, 0.3) mas yr ⁻¹
t_{back}	Uniform	[0, 10] Gyr
LSR Properties		
R_0	Fixed	8.0 kpc
$v_c(R_0)$	Fixed	237.0 km s ⁻¹
U_\odot	Fixed	11.1 km s ⁻¹
V_\odot	Fixed	12.24 km s ⁻¹
W_\odot	Fixed	7.25 km s ⁻¹

Table 3. The enclosed mass of the Milky Way as inferred from the stream precession modeling. We provide estimates at 50, 100, 150 and 200 kpc. Along with 68% and 95% confidence intervals.

r/kpc	$M(r)/10^{11} M_\odot$	$1\sigma/10^{11} M_\odot$	$2\sigma/10^{11} M_\odot$
50	2.9	0.4	0.9
100	4.1	0.7	1.6
150	4.9	1.0	2.4
200	5.6	1.2	3.0

lite pair onto a host may cause the heavier satellite to remain bound whilst the lighter satellite is ejected. Sales et al. (2007) find that that as many as a third of all satellites in their suite of simulations lie on such orbits. Although such extreme satellites may still be bound, the important point is that they do not constitute part of the virialized population. Mass estimates of the Milky Way using satellites depend on applying the virial theorem or the Jeans equations to the satellite populations assuming time-independence. Extreme satellites produced by three-body interactions should not be included in the sample.

Despite the advocacy of Boylan-Kolchin et al. (2013), there is another strong reason to exclude Leo I from the sample of bound satellites. Then, three independent methods of estimating the mass of the Milky Way – namely from the kinematics of distant halo stars (Deason et al. 2012;

Rashkov et al. 2013), the kinematics of the satellite galaxies (Watkins et al. 2010) and the modelling of the Sgr stream (this paper) – are all in good agreement. They all suggest that the total mass of the Milky Way is $\lesssim 1 \times 10^{12} M_\odot$. It is important to realise that high mass estimates for the Milky Way galaxy essentially depend on a single datapoint, namely the inclusion of Leo I in the sample of satellite galaxies modelled as a virialized population.

This has substantial implications for one of the alleged problems of Λ CDM, the “Too Big to Fail Problem”. Boylan-Kolchin et al. (2011) provide a lucid articulation of the problem. For simulated Milky Way analogues of mass $\sim 2 \times 10^{12} M_\odot$, the most massive subhaloes are too dense to correspond to any of the known satellite galaxies of the Milky Way. They typically have peak circular velocities of 30 km s⁻¹, which is too large to plausibly correspond to the most luminous dwarf spheroidal satellites of the Milky Way. Baryonic feedback does not appear to solve the problem entirely (Garrison-Kimmel et al. 2013), so many researchers have interpreted this as evidence for changing the nature of the dark matter particle to warm (Lovell et al. 2012) or self-interacting (Vogelsberger et al. 2012) or asymmetric (Zurek 2014). However, by far the simplest and likeliest way to resolve the “Too Big to Fail Problem” is to reduce the mass of the Milky Way Galaxy to $\sim 1 \times 10^{12} M_\odot$.

The work in this paper now provides a completely new and independent line of argument supporting a much leaner Milky Way Galaxy. Certainly out to ~ 100 kpc, the Sgr stream provides a particularly clean tool for mass estimation of the Milky Way. It is preferable to analyses of the satellite galaxies, as it circumvents the problem of sample contamination by unbound or unvirialized objects. It is preferable to analyses of the kinematics of halo stars as there is no mass-anisotropy degeneracy to frustrate mass determinations. We anticipate that – with increasing quality and quantity of data over the next few years – it will become the gold standard for mass measurements of the Milky Way.

ACKNOWLEDGEMENTS

The authors wish to thank the anonymous referee for a helpful and constructive report. The authors would also like to thank the members of the Cambridge “Streams” discussion club for their invaluable contribution. SG thanks the Science and Technology Facilities Council (STFC) for the award of a studentship. VB acknowledges financial support from the Royal Society. The research leading to these results has received funding from the European Research Council under the European Union’s Seventh Framework Programme (FP/2007-2013) / ERC Grant Agreement n. 308024.

REFERENCES

- Battaglia G., Helmi A., Morrison H., Harding P., Olszewski E. W., Mateo M., Freeman K. C., Norris J., Shectman S. A., 2005, MNRAS, 364, 433
- Belokurov V., Koposov S. E., Evans N. W., Peñarrubia J., Irwin M. J., Smith M. C., Lewis G. F., Gieles M., Wilkinson M. I., Gilmore G., Olszewski E. W., Niederste-Ostholt M., 2014, MNRAS, 437, 116

- Belokurov V., Zucker D. B., Evans N. W. et al., 2006, *ApJ*, 642, L137
- Binney J., Tremaine S., 2008, *Galactic Dynamics: Second Edition*. Princeton University Press
- Bovy J., 2014, *ArXiv e-prints*
- Bovy J., Allende Prieto C., Beers T. C., et. al. 2012, *ApJ*, 759, 131
- Boylan-Kolchin M., Bullock J. S., Kaplinghat M., 2011, *MNRAS*, 415, L40
- Boylan-Kolchin M., Bullock J. S., Sohn S. T., Besla G., van der Marel R. P., 2013, *ApJ*, 768, 140
- Brown W. R., Geller M. J., Kenyon S. J., Diaferio A., 2010, *AJ*, 139, 59
- Chakrabarti S., Quillen A., Chang P., Merritt D., 2014, *ArXiv e-prints*
- Deason A. J., Belokurov V., Evans N. W., An J., 2012, *MNRAS*, 424, L44
- Deason A. J., Belokurov V., Evans N. W., Koposov S. E., Cooke R. J., Peñarrubia J., Laporte C. F. P., Fellhauer M., Walker M. G., Olszewski E. W., 2012, *MNRAS*, 425, 2840
- Debattista V. P., Roškar R., Valluri M., Quinn T., Moore B., Wadsley J., 2013, *MNRAS*, 434, 2971
- Deg N., Widrow L., 2013, *MNRAS*, 428, 912
- Dehnen W., 2001, *MNRAS*, 324, 273
- Dinescu D. I., Girard T. M., van Altena W. F., López C. E., 2005, *ApJ*, 618, L25
- Eyre A., Binney J., 2009, *MNRAS*, 400, 548
- Eyre A., Binney J., 2011, *MNRAS*, 413, 1852
- Fellhauer M., Belokurov V., Evans N. W., 2006, *ApJ*, 651, 167
- Foreman-Mackey D., Hogg D. W., Lang D., Goodman J., 2013, *PASP*, 125, 306
- Garrison-Kimmel S., Rocha M., Boylan-Kolchin M., Bullock J. S., Lally J., 2013, *MNRAS*, 433, 3539
- Gnedin O. Y., Brown W. R., Geller M. J., Kenyon S. J., 2010, *ApJ*, 720, L108
- Helmi A., White S. D. M., 1999, *MNRAS*, 307, 495
- Hernquist L., 1990, *ApJ*, 356, 359
- Ibata R., Lewis G. F., Martin N. F., Bellazzini M., Correnti M., 2013, *ApJ*, 765, L15
- Ibata R. A., Gilmore G., Irwin M. J., 1994, *Nature*, 370, 194
- Johnston K. V., 1998, *ApJ*, 495, 297
- Koposov S. E., Belokurov V., Evans N. W., et. al. 2012, *ApJ*, 750, 80
- Koposov S. E., Belokurov V., Evans N. W., Gilmore G., Gieles M., Irwin M. J., Lewis G. F., Niederste-Ostholt M., Peñarrubia J., Smith M. C., Bizyaev D., Malanushenko E., Malanushenko V., Schneider D. P., Wyse R. F. G., 2012, *ApJ*, 750, 80
- Koposov S. E., Belokurov V., Wyn Evans N., 2013, *ApJ*, 766, 79
- Koposov S. E., Rix H.-W., Hogg D. W., 2010, *ApJ*, 712, 260
- Kunder A., Chaboyer B., 2009, *AJ*, 137, 4478
- Küpper A. H. W., Lane R. R., Heggie D. C., 2012, *MNRAS*, 420, 2700
- Lane R. R., Küpper A. H. W., Heggie D. C., 2012, *MNRAS*, 423, 2845
- Law D. R., Majewski S. R., 2010, *ApJ*, 714, 229
- Lin D. N. C., Lynden-Bell D., 1982, *MNRAS*, 198, 707
- Little B., Tremaine S., 1987, *ApJ*, 320, 493
- Lovell M. R., Eke V., Frenk C. S., Gao L., Jenkins A., Theuns T., Wang J., White S. D. M., Boyarsky A., Ruchayskiy O., 2012, *MNRAS*, 420, 2318
- Majewski S. R., Skrutskie M. F., Weinberg M. D., Osthheimer J. C., 2003, *ApJ*, 599, 1082
- Miyamoto M., Nagai R., 1975, *PASJ*, 27, 533
- Navarro J. F., Frenk C. S., White S. D. M., 1996, *ApJ*, 462, 563
- Newberg H. J., Yanny B., Grebel E. K., Hennessy G., Ivezić Ž., Martínez-Delgado D., Odenkirchen M., Rix H.-W., Brinkmann J., Lamb D. Q., Schneider D. P., York D. G., 2003, *ApJ*, 596, L191
- Niederste-Ostholt M., Belokurov V., Evans N. W., 2012, *MNRAS*, 422, 207
- Niederste-Ostholt M., Belokurov V., Evans N. W., Peñarrubia J., 2010, *ApJ*, 712, 516
- Peñarrubia J., Belokurov V., Evans N. W., Martínez-Delgado D., Gilmore G., Irwin M., Niederste-Ostholt M., Zucker D. B., 2010, *MNRAS*, 408, L26
- Price-Whelan A. M., Johnston K. V., 2013, *ApJ*, 778, L12
- Pryor C., Piatek S., Olszewski E. W., 2010, *AJ*, 139, 839
- Rashkov V., Pillepich A., Deason A. J., Madau P., Rockosi C. M., Guedes J., Mayer L., 2013, *ApJ*, 773, L32
- Sakamoto T., Chiba M., Beers T. C., 2003, *A&A*, 397, 899
- Sales L. V., Navarro J. F., Abadi M. G., Steinmetz M., 2007, *MNRAS*, 379, 1475
- Sanders J. L., 2014, *ArXiv e-prints*
- Sanders J. L., Binney J., 2013, *MNRAS*, 433, 1813
- Schönrich R., Binney J., Dehnen W., 2010, *MNRAS*, 403, 1829
- Slater C. T., Bell E. F., Schlafly E. F., Jurić M., Martin N. F., Rix H.-W., Bernard E. J., Burgett W. S., Chambers K. C., Finkbeiner D. P., Goldman B., Kaiser N., Magnier E. A., Morganson E. P., Price P. A., Tonry J. L., 2013, *ApJ*, 762, 6
- Smith M. C., Ruchti G. R., et. al. 2007, *MNRAS*, 379, 755
- Sofue Y., Honma M., Omodaka T., 2009, *PASJ*, 61, 227
- Sohn S. T., Besla G., van der Marel R. P., Boylan-Kolchin M., Majewski S. R., Bullock J. S., 2013, *ApJ*, 768, 139
- Springel V., 2005, *MNRAS*, 364, 1105
- Varghese A., Ibata R., Lewis G. F., 2011, *MNRAS*, 417, 198
- Vera-Ciro C., Helmi A., 2013, *ApJ*, 773, L4
- Vogelsberger M., Zavala J., Loeb A., 2012, *MNRAS*, 423, 3740
- Watkins L. L., Evans N. W., An J. H., 2010, *MNRAS*, 406, 264
- Wilkinson M. I., Evans N. W., 1999, *MNRAS*, 310, 645
- Xue X. X., Rix H. W., Zhao G., et. al. 2008, *ApJ*, 684, 1143
- Yoon J. H., Johnston K. V., Hogg D. W., 2011, *ApJ*, 731, 58
- Yu Q., Madau P., 2007, *MNRAS*, 379, 1293
- Zaritsky D., Olszewski E. W., Schommer R. A., Peterson R. C., Aaronson M., 1989, *ApJ*, 345, 759
- Zurek K. M., 2014, *Phys. Rep.*, 537, 91